

at the target location but not at a neighboring control location (Fig. 3, A to D, and fig. S12). These data imply that functional GABAARs are rapidly recruited to newly formed gephyrin clusters (Fig. 3, E and F). We also found that newly formed dendritic spines became functional, as indicated by glutamate uncaging-evoked AMPA receptor (AMPA)-mediated excitatory postsynaptic currents (uEPSCs) (Fig. 3, G and H). Thus, newly formed gephyrin clusters and dendritic spines gain functions by recruiting functional receptors.

To determine whether endogenous GABAergic synaptic activity also promotes both inhibitory and excitatory synaptogenesis, we used optogenetics to activate cortical interneurons. We first verified the efficacy of viral infection during early development (fig. S13 and movies S1 and S2) (21). We infected adeno-associated virus (AAV)-dfox. hChR2 (H134R)-mCherry after culturing cortical slices from somatostatin (SOM)-Cre mice (fig. S14); 3 to 5 days after viral infection, we delivered three rounds of blue light illumination (fig. S14). Photostimulation of ChR2-transfected SOM interneurons caused rapid formation of new gephyrin puncta and dendritic spines in young neurons, which was blocked by GABAzine; the same stimulation did not make induction in old slices (Fig. 4, A and B). To examine the proximity between presynaptic boutons and new gephyrin clusters or dendritic spines, we visualized both presynaptic SOM and postsynaptic pyramidal neurons (Fig. 4C) and found that the majority of gephyrin puncta and dendritic spines were formed close (<2 μ m) to the axonal boutons of SOM interneurons (Fig. 4D). Thus, GABA uncaging-induced synaptogenesis is triggered by the same mechanisms as synaptic GABA release under physiological conditions.

We next abolished GABA release by injecting AAV-containing tetanus toxin light chain (TeTxLC) inverted in a flip-excision (FLEX) cassette into EP3 culture from SOM-Cre mice (22). We confirmed that TeTxLC on its own prevented vesicle release (fig. S15) and did not affect synapse development (fig. S16). In TeTxLC-expressing SOM-Cre slices at EP11 and EP12, we found that the gephyrin puncta density in distal apical dendrites of layer 2/3 pyramidal neurons was reduced (Fig. 4, E and F, and fig. S17); this result implies that SOM-positive interneurons target distal apical dendrites of pyramidal neurons (23, 24). Spine density at apical dendrites was also reduced at EP7 (Fig. 4G), making spine numbers closer to those at EP3 or EP4 (fig. S18). Consistent with structural changes, TeTxLC expression reduced the frequency of both miniature IPSCs (mIPSCs) and miniature EPSCs (mEPSCs) in slices (Fig. 4, H and I) and in vivo (fig. S19). Thus, we suggest that early-developing GABAergic inputs from cortical interneurons control both inhibitory and excitatory circuitry during cortical development.

Our findings suggest that GABA sets the balance between inhibitory and excitatory synapses in early postnatal stages, laying the foundation for later circuit development (6, 25–27). Because the developing dendrites in our study did not have predetermined spots for inhibitory or excit-

atory synapses, localization of axonal boutons may be an early step in the precise formation of inhibitory and excitatory circuits (9, 28, 29). Thus, early-depolarizing GABA action appears to promote local synaptogenesis and shapes cortical circuitry during brain development.

REFERENCES AND NOTES

1. T. Branco, B. A. Clark, M. Häusser, *Science* **329**, 1671–1675 (2010).
2. C. Q. Chiu *et al.*, *Science* **340**, 759–762 (2013).
3. T. Hayama *et al.*, *Nat. Neurosci.* **16**, 1409–1416 (2013).
4. A. Losonczy, J. C. Magee, *Neuron* **50**, 291–307 (2006).
5. N. Spruston, *Nat. Rev. Neurosci.* **9**, 206–221 (2008).
6. P. Caroni, F. Donato, D. Müller, *Nat. Rev. Neurosci.* **13**, 478–490 (2012).
7. A. M. Hamilton *et al.*, *Neuron* **74**, 1023–1030 (2012).
8. Y. Kozorovitskiy, A. Saunders, C. A. Johnson, B. B. Lowell, B. L. Sabatini, *Nature* **485**, 646–650 (2012).
9. H. B. Kwon, B. L. Sabatini, *Nature* **474**, 100–104 (2011).
10. J. L. Chen *et al.*, *Neuron* **74**, 361–373 (2012).
11. D. van Versendaal *et al.*, *Neuron* **74**, 374–383 (2012).
12. M. Matsuzaki, T. Hayama, H. Kasai, G. C. Ellis-Davies, *Nat. Chem. Biol.* **6**, 255–257 (2010).
13. T. Kim, W. C. Oh, J. H. Choi, H. B. Kwon, *Proc. Natl. Acad. Sci. U.S.A.* **113**, E1372–E1381 (2016).
14. Y. Ben-Ari, *Neuroscience* **279**, 187–219 (2014).
15. C. Lüscher, L. Y. Jan, M. Stoffel, R. C. Malenka, R. A. Nicoll, *Neuron* **19**, 687–695 (1997).
16. J. Kirsch, H. Betz, *Nature* **392**, 717–720 (1998).
17. T. A. Hage, Z. M. Khaliq, *J. Neurosci.* **35**, 5823–5836 (2015).
18. G. W. Knott, A. Holtmaat, L. Wilbrecht, E. Welker, K. Svoboda, *Nat. Neurosci.* **9**, 1117–1124 (2006).
19. U. V. Nägerl, G. Köstinger, J. C. Anderson, K. A. Martin, T. Bonhoeffer, *J. Neurosci.* **27**, 8149–8156 (2007).
20. K. Zito, V. Scheuss, G. Knott, T. Hill, K. Svoboda, *Neuron* **61**, 247–258 (2009).

21. R. Batista-Brito, R. Machold, C. Klein, G. Fishell, *Cereb. Cortex* **18**, 2306–2317 (2008).
22. A. J. Murray *et al.*, *Nat. Neurosci.* **14**, 297–299 (2011).
23. S. X. Chen, A. N. Kim, A. J. Peters, T. Komiyama, *Nat. Neurosci.* **18**, 1109–1115 (2015).
24. J. Cichon, W. B. Gan, *Nature* **520**, 180–185 (2015).
25. M. Cane, B. Maco, G. Knott, A. Holtmaat, *J. Neurosci.* **34**, 2075–2086 (2014).
26. B. Dejanovic *et al.*, *PLOS Biol.* **12**, e1001908 (2014).
27. C. E. Flores *et al.*, *Proc. Natl. Acad. Sci. U.S.A.* **112**, E65–E72 (2015).
28. Z. J. Huang, *J. Physiol.* **587**, 1881–1888 (2009).
29. M. Miller, A. Peters, *J. Comp. Neurol.* **203**, 555–573 (1981).

ACKNOWLEDGMENTS

We thank members of the Kwon laboratory for discussion, E. Nedivi for TeTx-gephyrin, and H. Taniguchi for Flex-TeTxLC. Supported by the MPFI, a NARSAD Young Investigator grant, and NIH grants MH107460 (H.-B.K.) and MH081935 and DA017392 (P.E.C.). Supplementary materials contain additional data. Author contributions: W.C.O. and H.-B.K. conceived and designed the study; W.C.O. performed and analyzed all experiments except perforated patch-clamp recordings, which were performed and analyzed by S.L. and P.E.C.; W.C.O. prepared the figures; W.C.O. and H.-B.K. wrote the manuscript; and all authors revised the manuscript.

SUPPLEMENTARY MATERIALS

www.sciencemag.org/content/353/6303/1037/suppl/DC1
Materials and Methods
Figs. S1 to S19
Movies S1 and S2
References (30–36)

22 February 2016; accepted 3 August 2016
Published online 11 August 2016
10.1126/science.aaf5206

ION CHANNELS

Instantaneous ion configurations in the K⁺ ion channel selectivity filter revealed by 2D IR spectroscopy

Huong T. Kratochvil,¹ Joshua K. Carr,¹ Kimberly Matulef,² Alvin W. Annen,² Hui Li,³ Michał Maj,¹ Jared Ostmeier,³ Arnaldo L. Serrano,¹ H. Raghuraman,^{3*} Sean D. Moran,^{1†} J. L. Skinner,¹ Eduardo Perozo,^{3‡} Benoît Roux,^{3‡} Francis I. Valiyaveetil,^{2‡} Martin T. Zanni^{1‡}

Potassium channels are responsible for the selective permeation of K⁺ ions across cell membranes. K⁺ ions permeate in single file through the selectivity filter, a narrow pore lined by backbone carbonyls that compose four K⁺ binding sites. Here, we report on the two-dimensional infrared (2D IR) spectra of a semisynthetic KcsA channel with site-specific heavy (¹³C¹⁸O) isotope labels in the selectivity filter. The ultrafast time resolution of 2D IR spectroscopy provides an instantaneous snapshot of the multi-ion configurations and structural distributions that occur spontaneously in the filter. Two elongated features are resolved, revealing the statistical weighting of two structural conformations. The spectra are reproduced by molecular dynamics simulations of structures with water separating two K⁺ ions in the binding sites, ruling out configurations with ions occupying adjacent sites.

Ion channels that mediate the flux of K⁺ are responsible for determining the resting membrane potential and for the repolarization phase of action potentials of excitable cells (1). Ion permeation through all K⁺ channels

is characterized by high selectivity and throughput approaching the diffusion limit. These permeation properties are defined by the selectivity filter, a highly conserved structural element consisting of four K⁺ binding sites (S1 to S4, labeled

extracellular to intracellular) (Fig. 1B). During translocation, K⁺ coordination is carried out by main-chain carbonyl oxygens (plus a threonine side chain in S4) (2, 3).

The mechanism of ion permeation through the selectivity filter has been investigated using diverse experimental techniques such as radio-tracer flux assays, single-channel electrophysiological measurements, x-ray crystallography, and computational studies (3–11). These experiments are broadly supportive of a mechanism commonly referred to as “knock-on” permeation (4). This mechanism posits that the narrow selectivity filter is simultaneously occupied by two K⁺ ions in single file, either at sites S1 and S3 or at sites S2 and S4, with intervening water molecules (Fig. 1, C and D) (9–13). The approach of a third K⁺ ion from the intracellular side of the channel would advance the single file of alternating ions and water to the extracellular side, resulting in the net translocation of one K⁺ ion and one water molecule across the membrane. However, the experimental data are not sufficiently conclusive to rule out alternative models for the permeation mechanism (14–16). Of these, a recently proposed “hard-knock” permeation model suggests a very different mechanism. It postulates that the conductance of K⁺ channels arises from direct, short-range ion-ion collisions inside the filter, so that a pair of adjacent K⁺ ions occupy the selectivity filter at adjacent sites S2 and S3 with no intervening water molecules [0, S2, S3, 0] (17). In this model, permeation would take place when a third K⁺ ion enters the S4 binding site [0, S2, S3, S4], colliding directly with the S2/S3 ion pair to create the ion configuration [S1, S2, 0, S4]. Eventually, S1 would leave the filter and the K⁺ at S4 transitions to S3, starting over again (17). Here, we have used two-dimensional infrared (2D IR) spectroscopy and protein semisynthesis to test these permeation models, providing new experimental data on the ion and water configurations in the selectivity filter of the KcsA channel.

Atomic bond vibrations are sensitive to their electrostatic environment, so the frequencies are dictated by nearby ions and water as well as the structure and dynamics of the protein itself (18). The inherent time resolution of 2D IR spectroscopy is a few picoseconds, which implies that a 2D IR spectrum provides a nearly instantaneous snapshot of the dynamic channel and the content of the pore (19). In essence, it is a weighted average of the ion configurations and protein structural distributions (20). For the 2D IR

experiments, we used protein semisynthesis to selectively isotope-label the ion-binding sites in the selectivity filter. Using the native chemical ligation reaction, we assembled the KcsA protein from a synthetic peptide (residues 70 to 81) that encompasses the selectivity filter and two recombinant peptides corresponding to the rest of the protein. (21, 22). We introduced ¹³C¹⁸O labels on the backbone carbonyls of Val⁷⁶, Gly⁷⁷, and Gly⁷⁹ by using the appropriately labeled residues during synthesis of the peptide fragment

(Fig. 1B). The ¹³C¹⁸O labels cause a 65 cm^{−1} shift of the carbonyl frequency (amide I vibrations) (23), enabling us to spectroscopically isolate and probe the selectivity filter. Gly⁷⁷ and Val⁷⁶ probe the S1, S2, and S3 binding sites. These are good sites for labeling because these sites have different ion occupancies according to the two models. Labeling Gly⁷⁷ and Val⁷⁶ together makes the spectra particularly sensitive to ion configurations because of vibrational coupling between these two residues (24).

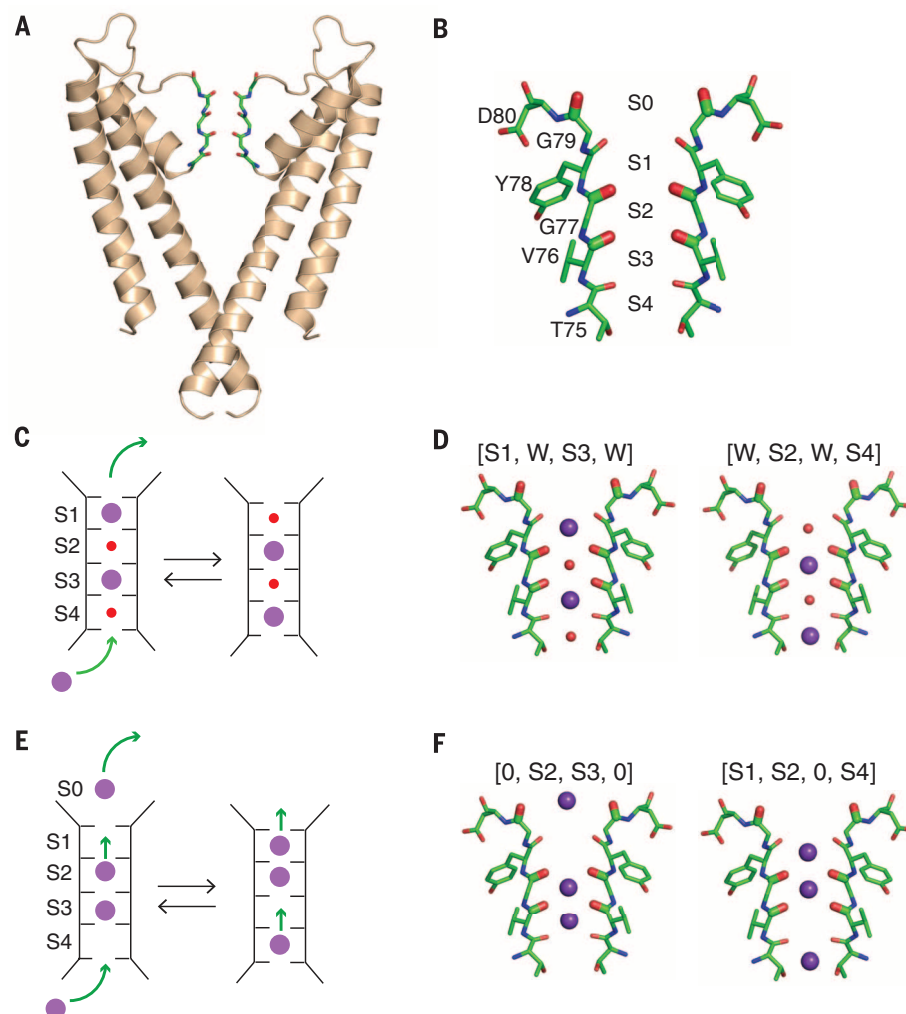


Fig. 1. Overview of ion permeation mechanisms of KcsA. (A) X-ray crystal structure of KcsA (PDB ID 1K4C), with two of the four protein subunits shown. (B) The selectivity filter of KcsA is lined with the carbonyl groups (oxygen in red) of four amino acids (Thr⁷⁵, Val⁷⁶, Gly⁷⁷, and Tyr⁷⁸). Amino acids that were ¹³C¹⁸O isotope labeled for the experiment are shown bolded (Val⁷⁶, Gly⁷⁷, and Gly⁷⁹). The binding sites (S1 to S4) span the selectivity filter. (C) Knock-on mechanism for potassium ion permeation through the channel. In this mechanism, K⁺ ions (purple) alternate with water molecules (red) and collectively move through the filter when a new K⁺ enters the filter. (D) The two most prominent ion-binding configurations for the knock-on mechanism used to simulate the 2D IR spectra: (left) [S1, W, S3, W] and (right) [W, S2, W, S4]. (E) The hard-knock model for ion conduction. When a K⁺ ion enters the S4 binding site, strong electrostatic repulsions simultaneously translocate two ions upward. No water is involved in this mechanism. (F) The two ion configurations used to simulate the 2D IR spectra: (left) [0, S2, S3, 0] and (right) [S1, S2, 0, S4]. Simulations for 97% of the ion configurations proposed by the hard-knock mechanism are shown in fig. S7. Single-letter abbreviations for the amino acid residues are as follows: A, Ala; C, Cys; D, Asp; E, Glu; F, Phe; G, Gly; H, His; I, Ile; K, Lys; L, Leu; M, Met; N, Asn; P, Pro; Q, Gln; R, Arg; S, Ser; T, Thr; V, Val; W, Trp; and Y, Tyr.

¹Department of Chemistry, University of Wisconsin-Madison, Madison, WI 53706, USA. ²Program in Chemical Biology, Department of Physiology and Pharmacology, Oregon Health and Science University, Portland, OR 97239, USA.

³Department of Biochemistry and Molecular Biology, The University of Chicago, Chicago, IL 60637, USA.

*Present address: Crystallography and Molecular Biology Division, Saha Institute of Nuclear Physics (SINP), Kolkata 700 064, India. †Present address: Department of Chemistry and Biochemistry, Southern Illinois University Carbondale, Carbondale, IL 62901, USA.

‡Corresponding author. Email: eperozo@uchicago.edu (E.P.); roux@uchicago.edu (B.R.); valiaye@ohsu.edu (F.I.V.); zanni@chem.wisc.edu (M.T.Z.)

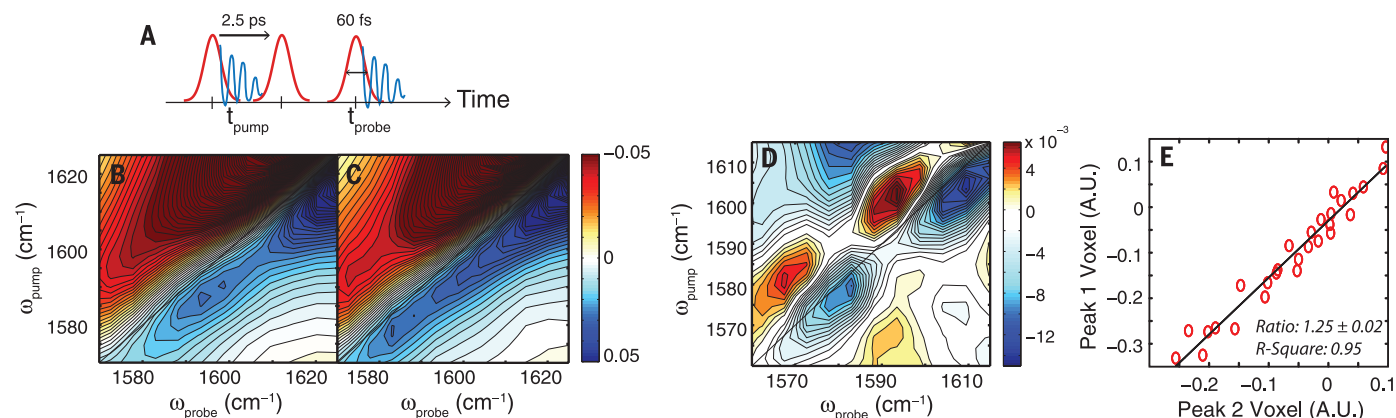


Fig. 2. Experimental 2D IR spectra of unlabeled and $^{13}\text{C}^{18}\text{O}$ -labeled KcsA at high potassium concentrations. (A) Pulse sequence for 2D IR spectrum with illustrated vibrational coherences (blue). Fourier transform of the coherence during t_{probe} to give the ω_{probe} axis, while the time between the pump pulses, t_{pump} , is computationally Fourier transformed to give the ω_{pump} axis. (B) 2D IR spectrum of unlabeled KcsA showing the absorption of side chains in the region where the isotope-labeled features are expected to appear. (C) 2D IR spectrum of labeled KcsA shows a 50% increase in intensity in this region,

consistent with absorption by the $^{13}\text{C}^{18}\text{O}$ labeled residues. (D) Subtraction of the unlabeled spectrum from the labeled spectrum yields two pairs of peaks. The bleaches (blue) appear at $(\omega_{\text{pump}}, \omega_{\text{probe}}) = (1603 \text{ cm}^{-1}, 1609 \text{ cm}^{-1})$ and $(1580 \text{ cm}^{-1}, 1582 \text{ cm}^{-1})$, respectively. (E) For every unique combination of difference spectra, the intensities of the 3 by 3 pixel array centered at the pixels for $(\omega_{\text{pump}}, \omega_{\text{probe}}) = (1603 \text{ cm}^{-1}, 1609 \text{ cm}^{-1})$ (peak 1) and $(1580 \text{ cm}^{-1}, 1582 \text{ cm}^{-1})$ (peak 2) were integrated, respectively. The slope of the fit yielded an intensity ratio of 1.25 ± 0.02 , with an R -square of 0.95.

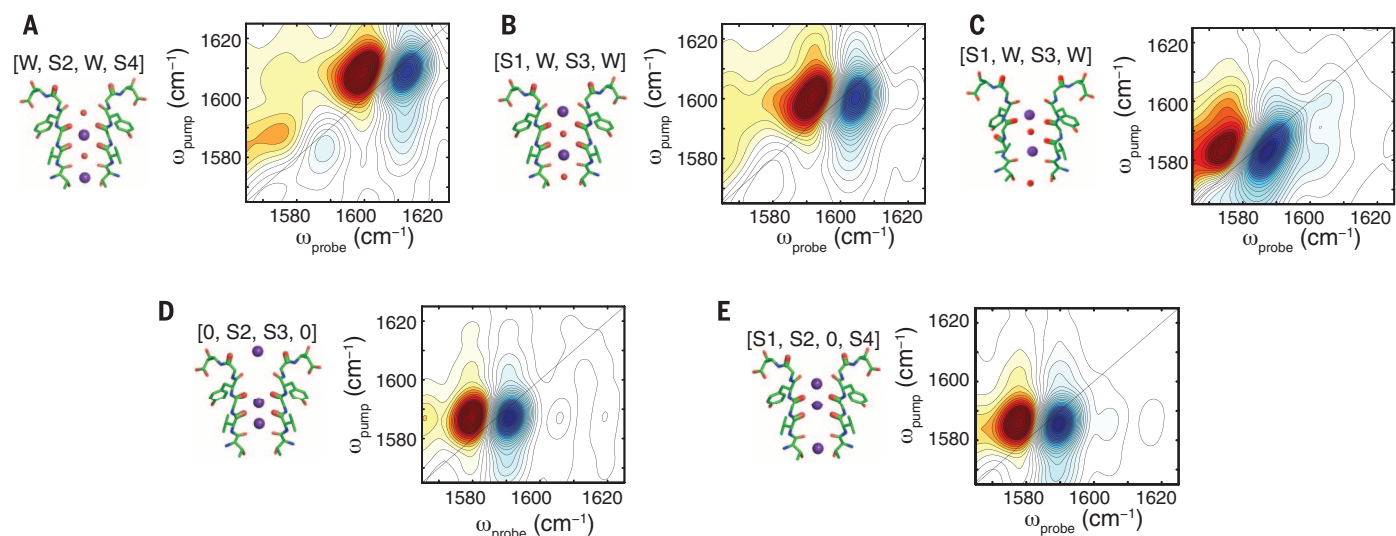


Fig. 3. Calculated 2D IR spectra to test proposed ion configurations of the KcsA selectivity filter. The calculated 2D IR spectra for the (A) [W, S2, W, S4], (B) [S1, W, S3, W], (C) [S1, W, S3, W] with a single Val⁷⁶ flip, (D) [0, S2, S3, 0], and (E) [S1, S2, 0, S4] K^+ binding configurations of the labeled KcsA filter from MD simulations using a K^+ charge profile described in (35). In (A), we have the spectrum for the [W, S2, W, S4] ion-binding configuration in which all of the Val⁷⁶ residues point into the filter. In this case, we observe peaks at $(\omega_{\text{pump}}, \omega_{\text{probe}}) = (1608 \text{ cm}^{-1}, 1612 \text{ cm}^{-1})$. (B) For the [S1, W, S3, W] configuration,

we see a similar spectrum with $(\omega_{\text{pump}}, \omega_{\text{probe}}) = (1600 \text{ cm}^{-1}, 1604 \text{ cm}^{-1})$. (C) For the [S1, W, S3, W] ion configuration of the Val⁷⁶-flipped state, we get a pair of inhomogeneous peaks at $(\omega_{\text{pump}}, \omega_{\text{probe}}) = (1583 \text{ cm}^{-1}, 1587 \text{ cm}^{-1})$. (D) and (E) are the calculated 2D IR spectra of the [0, S2, S3, 0] and [S1, S2, 0, S4] binding configurations, respectively. In (E), we observe a single homogeneous peak at $(\omega_{\text{pump}}, \omega_{\text{probe}}) = (1587 \text{ cm}^{-1}, 1591 \text{ cm}^{-1})$, which is similar to the homogeneous peak we observe in (F) at $(\omega_{\text{pump}}, \omega_{\text{probe}}) = (1585 \text{ cm}^{-1}, 1589 \text{ cm}^{-1})$. The spectra have been normalized for visualization purposes.

Shown in Fig. 2C is the 2D IR spectrum of labeled KcsA. This spectrum was collected using the pulse sequence shown in Fig. 2A. This approach is analogous to that used in 2D nuclear magnetic resonance spectroscopy, but probing vibrational modes. This pulse sequence produces an infrared signal that oscillates as a function of the time delay between the pump pulses and after the probe pulse, respectively. The sig-

nal is Fourier transformed along these two time axes to give a 2D IR spectrum that correlates the two frequency axes. The spectrum in Fig. 2C is shown in the region that the $^{13}\text{C}^{18}\text{O}$ -labeled carbonyls absorb [full spectra are shown in the supplementary materials (SM)]. Acidic side chains also absorb in this region, creating a background (25, 26). To remove the background, we also measured a KcsA sample without isotope

labels under identical conditions. The intensity of the unlabeled KcsA spectrum is about 50% lower in this region, which is approximately what we would expect based on the ratio of labels to acidic side chains.

Figure 2D shows the difference spectrum generated by subtracting Fig. 2, B and C. It contains two pairs of oppositely signed peaks, with blue, negative peaks corresponding to the

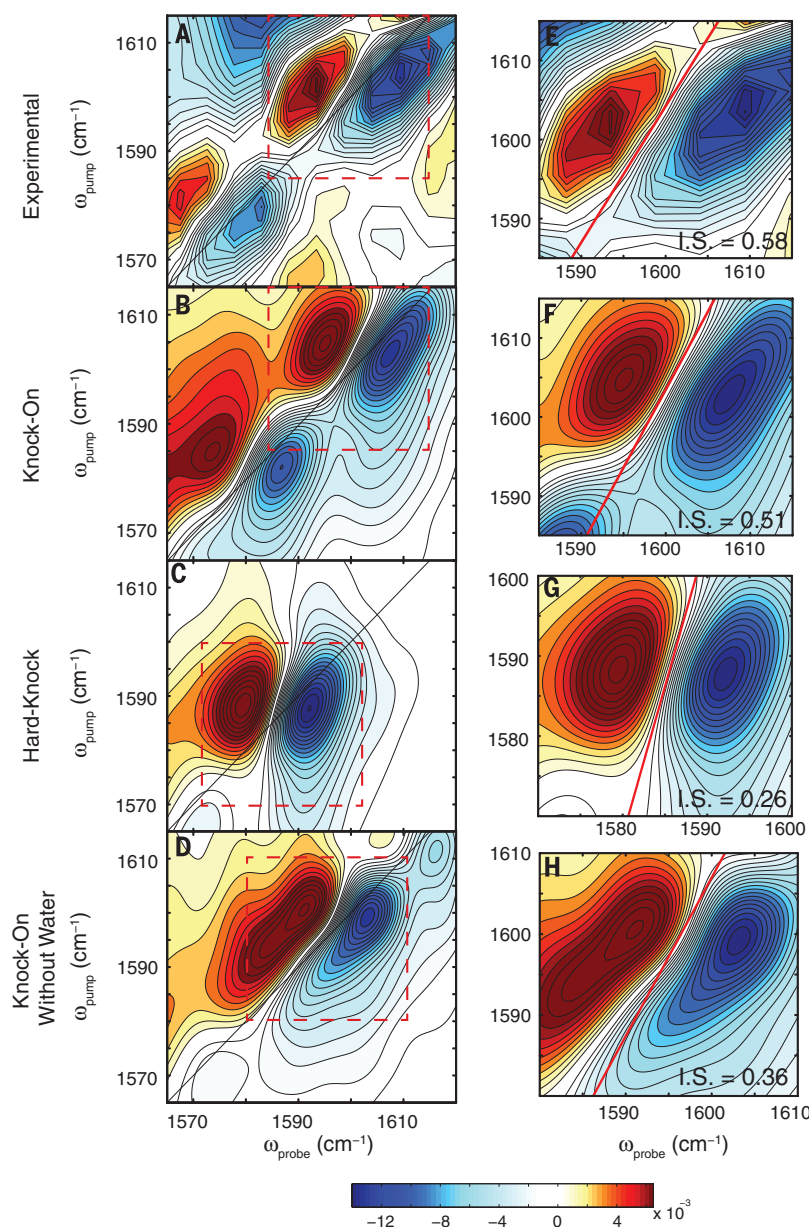


Fig. 4. Comparison of 2D IR experimental spectrum to the simulated spectra of the knock-on models (with and without water) and the hard-knock model. (A) Experimental difference spectrum shown in Fig. 2C. (B) Simulated 2D IR spectrum for the knock-on model with water generated by a weighted average of the [W, S2, W, S4], [S1, W, S3, W], and Val⁷⁶ flipped [S1, W, S3, W] ion configurations in a ratio of 0.3:0.3:0.4, respectively. The simulated spectrum agrees well with peak positions, 2D lineshapes, and intensity ratio. (C) Simulated 2D IR spectrum for the hard-knock model from a weighted average of [0, S2, S3, 0] and [S1, S2, 0, S4], along with other hard-knock states (see SM). (D) Simulated 2D IR spectrum of the knock-on model with water removed with the same ratios of states used to match experiment (Fig. 4B). No linear combination of these states without water (see fig. S14) reproduces the experimental spectrum. Therefore, water must be present within the filter. (E to H) Zoom-ins of the high-frequency peak of each spectra. The nodal line slopes are illustrated by red lines with values of the inverse slope (I.S.).

0→1 vibrational transition and red, positive peaks corresponding to the 1→2 vibrational transition. For each isotope label, our pulse sequence will create a pair of oppositely signed peaks, with the negative peak on the diagonal. Thus, the difference spectrum resolves two vibrational fea-

tures, which we refer to by their frequencies along the y axis, $\omega_{\text{pump}} = 1603 \text{ cm}^{-1}$ and 1580 cm^{-1} . The frequencies reflect the magnitude of the electric fields inside the filter as well as the coupling between residues set by the backbone structure (27, 28). The two pairs of peaks have

very different frequencies, with a peak separation of 23 cm^{-1} along ω_{pump} , indicating that there is either a single protein structure or ion configuration that has distinct electrostatics at the separate binding sites or a weighted average of two conformations with very different electrostatics. A statistical analysis is presented in the SM that addresses reproducibility and statistical significance. A portion of this analysis is shown in Fig. 2E, which plots the intensity of the 1603 and 1580 cm^{-1} peaks for every combination of foreground and background spectra that we collected. If the experimental peaks were not reproducible, then this plot would be uncorrelated. Instead, a strong correlation is observed with a slope of 1.25 ± 0.02 , which equals the relative intensities of the two peaks. As we show below, the relative intensity gives the statistical weighting of ion channel structures.

To determine whether these experimental features can be explained by either of the two permeation models described above, we conducted molecular dynamics (MD) simulations and computed 2D IR spectra for all relevant ion configurations (see SM for methods). Shown in Fig. 3, A and B, are 2D IR spectra calculated for each of the two multi-ion configurations predicted to occur during ion conduction according to the knock-on model, [W, S2, W, S4] and [S1, W, S3, W]. The spectrum of the [W, S2, W, S4] ion configuration has an intense pair of peaks at 1608 cm^{-1} . A similar spectrum is predicted for the [S1, W, S3, W] ion-binding configuration, albeit centered at 1600 cm^{-1} . Simulations of the individual residues reveal that Val⁷⁶, which is coordinating the S2 K⁺ ion, is mostly responsible for the frequency and the spectral intensity that we observe in this ion-binding configuration (see SM). MD simulations also predict that the Val⁷⁶ carbonyl is often flipped outward (16, 29), away from the pore (see Fig. 3C) when the ions are in the [S1, W, S3, W] configuration. Simulations of that structure predict a pair of peaks that are much lower in frequency, absorbing at 1583 cm^{-1} . The flipped state is not predicted to exist for the [W, S2, W, S4] ion configuration (29).

Shown in Fig. 3, C and D, are the calculated 2D IR spectra for two of the ion configurations of the new hard-knock model, [0, S2, S3, 0] and [S1, S2, 0, S4]. Both ion configurations predict nearly the same 2D IR spectrum, with frequencies of 1587 and 1585 cm^{-1} . Ions in the channel tend to shift carbonyls to lower frequencies because of their charge, which is why this model predicts low frequencies for both ion configurations. The hard-knock model also contains other ion configurations in its mechanism, whose computed spectra are given in the SM (fig. S7). The predicted spectra for the ion configuration corresponding to the knock-on and the hard-knock models are very different from one another in both peak frequency and 2D lineshape.

For comparison to experiment, the simulated spectra of the structures in the knock-on model ([W, S2, W, S4]:[S1, W, S3, W]:flipped[S1, W, S3, W]) were added at a ratio of 0.3:0.3:0.4 to match the relative intensities in the experimental spectra

(the experimental peaks have a ratio of 1.25 ± 0.02 , from Fig. 2E). The agreement between the knock-on model and experiment is good (Fig. 4B versus 4A), especially considering that the only adjustable parameters in these calculations are the relative ratios. We also added together the 2D spectra for 97% of the ion configurations predicted from the hard-knock model (Fig. 3, D and E, and fig. S7), which gives the spectrum in Fig. 4C (17). The agreement to experiment is poor; the simulations only predict one set of peaks instead of two. There is no linear combination of hard-knock ion configurations or structures that can match the experiment. We have also explored whether the ion configurations of the hard-knock model occur, albeit less frequently, along with the configurations for the knock-on states. To do so, we added the spectra of the hard-knock configurations to the knock-on states (fig. S12). We estimate that there cannot be more than 15% of the states in the hard-knock configuration, because increasing the population beyond this limitation decreases the frequency separation and changes the 2D lineshapes of the peaks. Therefore, our data are consistent with ion distributions in the filter predicted by the classic knock-on model but not the hard-knock model proposed more recently.

An analysis of the 2D lineshapes corroborates our conclusions and provides additional insights. The calculated 2D lineshapes are elongated for the knock-on model and rounder for the hard-knock model (Fig. 4, B and D, respectively). Two-dimensional lineshapes are elongated along the diagonal when there is a heterogeneous subset of frequencies—and, accordingly, structures—each with its own set of electric fields. In essence, the 2D lineshapes measure the structural distribution of the selectivity filter for each ion configuration (30). Shown in Fig. 4, E to H (red lines), are nodal line slopes that quantify the inhomogeneity of the 2D lineshapes. The experiment and simulations of the knock-on model both have inverse slopes of about 0.6, whereas the hard-knock model has an inverse slope of about 0.3 (see table S3). To test the effect of water on the knock-on spectra, we reran the molecular dynamics simulations without water in the selectivity filter (Fig. 4D). The simulations predict that the high-frequency peak bifurcates because the [0, S2, 0, S4] ion-binding configuration blueshifts 4 cm^{-1} (see fig. S13), and the inverse slope is too small. There are no linear combinations of the knock-on states without water that can reproduce the experimental spectrum in Fig. 4B. Thus, water must be present in the channel to reproduce the experimental 2D lineshape. It follows that during ion conduction, one water molecule is transported for each K^+ ion, in accord with streaming potential (9, 12, 13).

Analyzing the angles of the isotope-labeled carbonyls inside the selectivity filter, we found that removing the water from the knock-on model reduces the angular distribution by as much as 36% (see fig. S11). The hard-knock model, which also lacks water, has a similarly narrow angular distribution. Without the water, the high

positive charge inside the filter causes a more rigid protein conformation and less dynamic K^+ ions, similar to experiments on K^+ binding to model peptides (24).

Because the temporal resolution of 2D IR spectroscopy is orders of magnitude shorter than the time scales for ion permeation, we can determine from the 2D IR spectra the relative populations of each of these ion-binding states. The experimental peaks have a ratio of 1.25 ± 0.02 from Fig. 2E. It follows that the relative equilibrium population of the [W, S2, W, S4], [S1, W, S3, W], and Val⁷⁶-flipped [S1, W, S3, W] ion configurations required to account for differences in lineshape and transition dipole strengths can be determined to be 30%, 30%, and 40%, respectively. The [W, S2, W, S4] and [S1, W, S3, W] ion configurations are equally populated, to within 5% of each other, which is in agreement with the ratio of states found in x-ray diffraction studies (6, 9). Thus, the Val⁷⁶-flipped [S1, W, S3, W] ion configuration accounts for roughly 40% of the states at equilibrium. This flipped state has been reported in MD simulations (29) but has not been observed with x-ray crystallography.

The ultrafast time resolution of 2D IR spectroscopy provides an opportunity to test short-lived configurations extracted from MD simulations. Because the 2D IR time resolution of 1 to 2 ps is faster than almost all protein dynamics, the spectrum reports on the instantaneous distribution of ions, water, and protein structures. As a result, 2D IR spectroscopy provides a means to test protein conformations observed in crystal structures and to empirically refine simulations to effectively reweight configurations. Energy differences on the order of $k_B T$ ($k_B T = 0.593 \text{ kcal mol}^{-1}$ at 298 K) are below the accuracy of current force fields (37), so simulations generated from different force fields could lead to different conclusions (37). Rather than test individual hypotheses, one might also simulate 2D IR spectra generated from Markov state models to analyze entire trajectories (32, 33). Essential for this study was the ability to selectively introduce $^{13}\text{C}^{18}\text{O}$ isotope labels into the ion-binding sites in the filter. Advances in the semisynthesis methodology or, alternatively, the use of nonsense suppression approaches have widely expanded the range of membrane proteins that can be selectively labeled and therefore investigated using 2D IR spectroscopy (34). We anticipate that the combination of these new labeling methods, molecular dynamics, and 2D IR spectroscopy will be an important addition to the tool kit presently used to investigate the functional mechanisms that operate in membrane proteins.

REFERENCES AND NOTES

- B. Hille, *Ion Channels of Excitable Membranes* (Sinauer, Sunderland, MA, 2001).
- L. Heginbotham, T. Abramson, R. MacKinnon, *Science* **258**, 1152–1155 (1992).
- D. A. Doyle et al., *Science* **280**, 69–77 (1998).
- A. L. Hodgkin, R. D. Keynes, *J. Physiol.* **128**, 61–88 (1955).
- S. Uysal et al., *Proc. Natl. Acad. Sci. U.S.A.* **106**, 6644–6649 (2009).
- J. H. Morais-Cabral, Y. Zhou, R. MacKinnon, *Nature* **414**, 37–42 (2001).

- A. N. Thompson et al., *Nat. Struct. Mol. Biol.* **16**, 1317–1324 (2009).
- S. Y. Noskov, S. Bernèche, B. Roux, *Nature* **431**, 830–834 (2004).
- Y. Zhou, R. MacKinnon, *J. Mol. Biol.* **333**, 965–975 (2003).
- S. Bernèche, B. Roux, *Nature* **414**, 73–77 (2001).
- S. Bernèche, B. Roux, *Proc. Natl. Acad. Sci. U.S.A.* **100**, 8644–8648 (2003).
- C. Alcayaga, X. Cecchi, O. Alvarez, R. Latorre, *Biophys. J.* **55**, 367–371 (1989).
- M. Iwamoto, S. Oiki, *J. Neurosci.* **31**, 12180–12188 (2011).
- J. Åqvist, V. Luzhkov, *Nature* **404**, 881–884 (2000).
- S. Furini, C. Domene, *Proc. Natl. Acad. Sci. U.S.A.* **106**, 16074–16077 (2009).
- P. W. Fowler, E. Abad, O. Beckstein, M. S. Sansom, *J. Chem. Theory Comput.* **9**, 5176–5189 (2013).
- D. A. Köpfer et al., *Science* **346**, 352–355 (2014).
- S. D. Fried, S. Bagchi, S. G. Boxer, *J. Am. Chem. Soc.* **135**, 11181–11192 (2013).
- A. Ghosh, J. Qiu, W. F. DeGrado, R. M. Hochstrasser, *Proc. Natl. Acad. Sci. U.S.A.* **108**, 6115–6120 (2011).
- P. Stevenson et al., *J. Phys. Chem. B* **119**, 5824–5831 (2015).
- F. I. Valiyaveetil, R. MacKinnon, T. W. Muir, *J. Am. Chem. Soc.* **124**, 9113–9120 (2002).
- A. G. Komarov, K. M. Linn, J. J. Devereaux, F. I. Valiyaveetil, *ACS Chem. Biol.* **4**, 1029–1038 (2009).
- J. Torres, A. Kukol, J. M. Goodman, I. T. Arkin, *Biopolymers* **59**, 396–401 (2001).
- Z. Ganim, A. Tokmakoff, A. Vaziri, *New J. Phys.* **13**, 113030 (2011).
- A. Barth, *Prog. Biophys. Mol. Biol.* **74**, 141–173 (2000).
- A. Barth, C. Zscherp, *Q. Rev. Biophys.* **35**, 369–430 (2002).
- H. Kim, M. Cho, *Chem. Rev.* **113**, 5817–5847 (2013).
- Y. S. Kim, R. M. Hochstrasser, *J. Phys. Chem. B* **113**, 8231–8251 (2009).
- S. Bernèche, B. Roux, *Structure* **13**, 591–600 (2005).
- P. Hamm, M. T. Zanni, *Concepts and Methods of 2D Infrared Spectroscopy* (Cambridge University Press, New York, 2011).
- H. Li et al., *J. Phys. Chem. B* **119**, 9401–9416 (2015).
- C. R. Baiz et al., *Biophys. J.* **106**, 1359–1370 (2014).
- C. R. Schwantes, V. S. Pande, *J. Chem. Theory Comput.* **9**, 2000–2009 (2013).
- L. Leisle, F. Valiyaveetil, R. A. Mehl, C. A. Ahern, in *Novel Chemical Tools to Study Ion Channel Biology*, C. Ahern, S. Pless, Eds. (Springer, New York, 2015), vol. 869, chap. 7, pp. 119–151.
- S. Kraszewski, C. Boiteux, C. Ramseier, C. Girardet, *Phys. Chem. Chem. Phys.* **11**, 8606–8613 (2009).

ACKNOWLEDGMENTS

This research was supported by U.S. National Institutes of Health grant NIH DK79895 (H.T.K., A.L.S., S.D.M., M.M., and M.T.Z.), the University of Wisconsin Foundation (J.K.C. and J.L.S.), NIH R01-GM062342 (H.L. and B.R.), NIH GM087546 (K.M., A.W.A., and F.I.V.), NIH R01-GM057846 (E.P. and H.R.), and the Membrane Protein Structural Dynamics Consortium U54-GM087519. F.I.V. and A.W.A. thank members of the Xiao group for advice on chemical synthesis. M.T.Z. is an owner of PhaseTech Spectroscopy, Inc. Additional materials, methods, and supplementary text detailing the data reported in this paper can be found in the supplementary materials.

SUPPLEMENTARY MATERIALS

www.sciencemag.org/content/353/6303/1040/suppl/DC1
Materials and Methods
Supplementary Text
Figs. S1 to S13
Tables S1 to S3
References (36–59)

14 May 2016; accepted 3 August 2016
10.1126/science.aag1447

Instantaneous ion configurations in the K⁺ ion channel selectivity filter revealed by 2D IR spectroscopy

Huong T. Kratochvil, Joshua K. Carr, Kimberly Matulef, Alvin W. Annen, Hui Li, Michal Maj, Jared Ostmeyer, Arnaldo L. Serrano, H. Raghuraman, Sean D. Moran, J. L. Skinner, Eduardo Perozo, Benoît Roux, Francis I. Valiyaveetil and Martin T. Zanni

Science **353** (6303), 1040-1044.
DOI: 10.1126/science.aag1447

ARTICLE TOOLS

<http://science.sciencemag.org/content/353/6303/1040>

SUPPLEMENTARY MATERIALS

<http://science.sciencemag.org/content/suppl/2016/08/31/353.6303.1040.DC1>

REFERENCES

This article cites 56 articles, 11 of which you can access for free
<http://science.sciencemag.org/content/353/6303/1040#BIBL>

PERMISSIONS

<http://www.sciencemag.org/help/reprints-and-permissions>

Use of this article is subject to the [Terms of Service](#)